Controlled thickness and morphology for highly efficient inverted planar heterojunction perovskite solar cells

Article *in* Nanoscale · May 2015

DOI: 10.1039/C5NR01988E

9 authors, including:

Zhaoxin Wu
Xi'an Jiaotong University
114 PUBLICATIONS **981** CITATIONS
SEE PROFILE

Hua Dong
Xi'an Jiaotong University
35 PUBLICATIONS **129** CITATIONS
SEE PROFILE

Jiao Bo
Xi'an Jiaotong University
65 PUBLICATIONS **311** CITATIONS
SEE PROFILE

Xun Hou
Xi'an Jiaotong University
377 PUBLICATIONS **2,244** CITATIONS
SEE PROFILE

Nanoscale

PAPER

View Article Online
View Journal | View Issue

Cite this: *Nanoscale*, 2015, **7**, 10699

Controlled thickness and morphology for highly efficient inverted planar heterojunction perovskite solar cells†

Jun Xi,‡[a] Zhaoxin Wu,*‡[a] Hua Dong,[a] Bin Xia,[a] Fang Yuan,[a] Bo Jiao,[a] Lixin Xiao,*[b] Qihang Gong[b] and Xun Hou[a]

Received 28th March 2015,
Accepted 11th May 2015

DOI: 10.1039/c5nr01988e

www.rsc.org/nanoscale

Recently, inverted planar heterojunction (PHJ) perovskite solar cells have been developed rapidly by numerous preparations and relative optimizations. Sequential solution deposition is easy to manipulate but it is difficult to control the thickness and morphology of perovskite films. In this article, we report an improved sequential deposition, named twice dipping-vapor solution deposition (TD-VSD) technology, to accurately achieve superior perovskite films. It is demonstrated that the morphology of perovskite films depended on the substrate temperatures as well as the dipping times. The resulting solar cells showed the power conversion efficiency as high as 11.77% based on the ideal thickness and morphology. This work provides a simple but effective fabrication to well control the perovskite films and enhance the power conversion efficiency for inverted PHJ solar cells.

Introduction

Since Miyasaka *et al.* first achieved a promising power conversion efficiency (PCE) using organolead trihalide perovskites,[1] hybrid organic/inorganic $MAPbX_3$ (MA = CH_3NH_3, X = I, Br or Cl) have drawn tremendous attention all over the photovoltaic field in recent years. Numerous superior properties of perovskites as absorbers, including a suitable band gap (about 1.5 eV), exceptional absorption of visible light, long range carrier transport and high carrier mobilities, have been demonstrated by a series of mechanism studies.[2–5] Moreover, the state of the art perovskite solar cells with a PCE of 19.3% greatly overwhelmed other solar cells (such as organic photovoltaics (OPV) and dye-sensitized solar cells (DSSC)).[6]

Meso-superstructured perovskite sensitized solar cells, evolved from DSSCs, showed relatively high PCEs for several years,[7,8] and have been rapidly accelerated by a solution process.[9–12] Despite the advantages of easy-manipulation, some drawbacks and limitations of this structure are disappointing: the high treatment temperature for mesoporous scaffolds, costly hole transportation materials 2,2′,7,7′-tetrakis-(*N*,*N*-di-*p*-methoxyphenylamine)9,9′-spirobifluorene (spiro-OMeTAD) and poor reproducibility.[12,13] Surprisingly, low temperature planar heterojunction (PHJ) structures sandwiched by p-type and n-type layers, arising from organic film devices, have exhibited better device performances, overcome these issues and could be utilized for commercialization even for flexible devices.[14–17] However, the efficiency losses, structure defects and carrier recombination at the interfaces lead to worse performances.[15] Thus, a lot of optimizations have been reported as follows: substitution of a p-type layer (such as NiO, graphene oxide, CuSCN and so on),[18–23] interface modification,[24,25] optimization of the perovskite procedure solution,[26,27] and vacuum deposition.[28–31] There is no doubt that the aim of the above optimization is to support continuous and smooth perovskite films.

In previous reports, three fabrications of perovskite films were employed.[7,32,33] (1) Dual-source vacuum deposition contributes to a compact and flat film, but needs advanced apparatus and is difficult to detect the deposition rates of CH_3NH_3I.[28] (2) One-step spin-coating easily forms incomplete and non-uniform perovskite films.[10,34,35] What's more, a critical environment is inevitable for this process. (3) Sequential solution deposition leads to large crystalline grains; it can hardly control the crystal sizes and results in an inferior device performance.[36] Especially for fabricating inverted PHJ structures, thicker n-type layers (such as C60, PCBM and

[a]*Key Laboratory of Photonics Technology for information, Key Laboratory for Physical Electronics and Devices of the Ministry of Education, School of Electronic and Information Engineering, Xi'an Jiaotong University, Xi'an 710049, P. R. China. E-mail: zhaoxinwu@mail.xjtu.edu.cn; Tel: +86-29-82664867*

[b]*State Key Laboratory for Mesoscopic Physics and Department of Physics, Peking University, Beijing 100871, P. R. China. E-mail: xiao66@pku.edu.cn*

†Electronic supplementary information (ESI) available. See DOI: 10.1039/c5nr01988e

‡These authors contributed equally to this work.

other fullerene derivatives) are hardly realized compared to spiro-OMeTAD (in TiO_2 mesoporous structures), whereas they are indispensible for the rough perovskite films by sequential solution deposition.[8,24] Recently, Tang *et al.* have realized a PCE of 7.6% by sequential deposition.[22] Furthermore, a higher PCE of 9.11% was reported with NiO nanocrystals by the group of Yang.[23] But thinner n-type layers would improve the conductivity and accordingly lead to a better device performance.[37–39] Consequently, an appropriate thickness of n-type layers is also paramount to achieve the preferable device performance. It is not easy, however, to obtain excellent device parameters for PHJ structures by sequential deposition due to the demerits mentioned above.

In this work, we establish an improved sequential deposition for inverted PHJ perovskite solar cells by the vapor solution deposition (VSD) approach, which is dipping vapor deposition (VD) PbI_2 films into a CH_3NH_3I solution for deposition. We find that twice dipping VSD (TD-VSD) is more sufficient and effective than once dipping VSD (OD-VSD), but third dipping VSD (T'D-VSD) is detrimental for a perovskite film. Consequently, TD-VSD is favorable for PHJ devices. It is notable that DMF will dissolve part of PEDOT:PSS films by traditional sequential solution deposition.[23] The VD PbI_2 could protect the PEDOT:PSS films, and fortunately the resulting $CH_3NH_3PbI_3$ thickness can be precisely controlled by vacuum deposition. In addition, the substrate temperatures could impact the perovskite morphology. The champion solar cells show power conversion efficiencies as high as 11.77% by further optimizing other conditions of the technology, which are superior to similar sequential deposition with the same architectures (about 5% to 9%).[22,23] We also reveal the importance of the absorption and morphology for the inverted PHJ perovskite solar cells.

Results and discussion

OD-VSD for perovskite solar cells

The schematic procedure of OD-VSD technology (Fig. 1a) is similar to that of the traditional sequential solution deposition, and a detailed process can be found in the Experimental section. The device structure and the energy level diagram of PHJ solar cells developed in our work are shown in Fig. 1b and c. PbI_2 powders were heated to its sublimation temperature to form transport yellow films. The PbI_2 film was further characterized by X-ray diffraction (XRD) in Fig. 2a. The predominant peak at 12.6° of the XRD pattern is ascribed to the (001) lattice plane of the crystallized PbI_2, and the inset scanning electron microscopy (SEM) image of Fig. 2a shows a continuous and smooth PbI_2 film consisting of a multitude of homogeneous crystals. The substrates were heated at different temperatures (including RT, 40 °C, 50 °C, 60 °C, 70 °C and 80 °C) for 2 min, and then immersed in a CH_3NH_3I solution to form a dark brown perovskite ($CH_3NH_3PbI_3$). On account of the volatility of DCM (dichloromethane) and the poor solubility of perovskites in DCM,[40] the sample ITO/PEDOT:PSS/

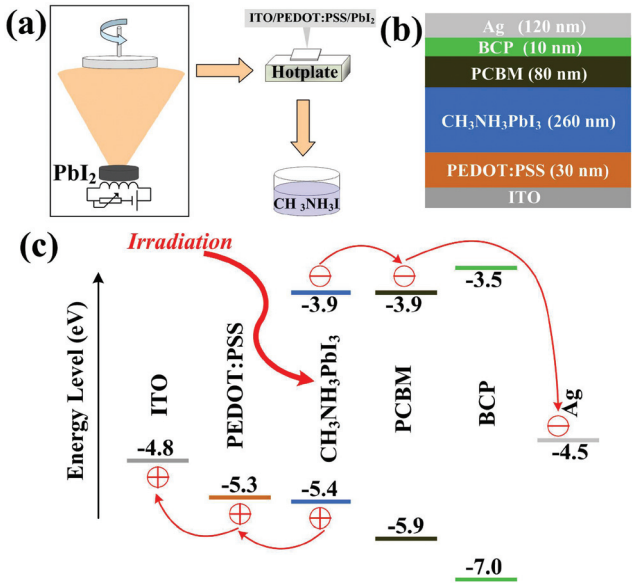

Fig. 1 (a) Schematic procedure of OD-VSD technology. (b) Device structure of the prepared PHJ solar cells. (c) Corresponding energy levels diagram as well as carrier transportation under solar illumination.

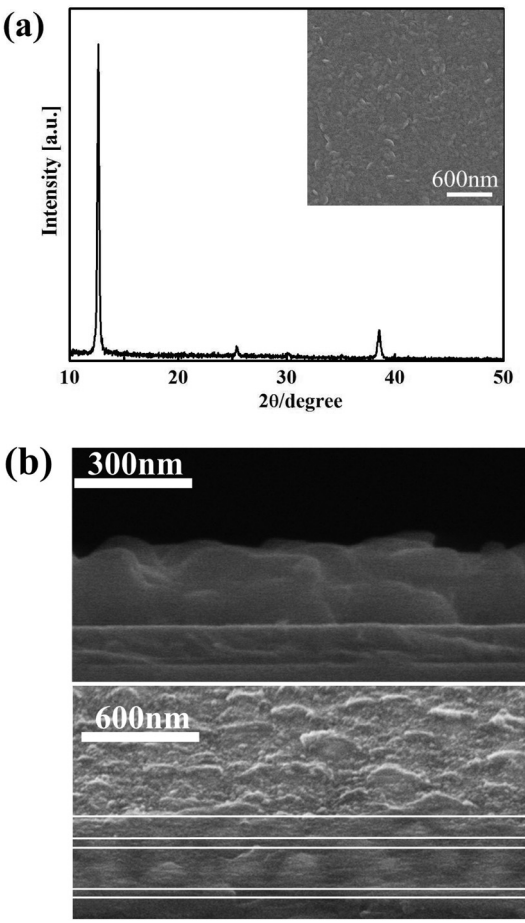

Fig. 2 (a) XRD pattern of the VD PbI_2 film (inset: SEM images). (b) The cross-sectional SEM images of the $CH_3NH_3PbI_3$ film and the device structure.

$CH_3NH_3PbI_3$ was cleaned with IPA (2-propanol) and DCM sequentially to eliminate the MAI trace.

Compared with traditional sequential solution deposition, this process can be operated easily and is time-saving as annealing is avoided. The top image of Fig. 2b exhibits an approximately 260 nm thickness of a continuous $CH_3NH_3PbI_3$ film. The prepared perovskite was next protected with 80 nm PCBM by spin-coating. Eventually, the devices were deposited with 10 nm BCP and 120 nm Ag cathode sequentially to complete. The BCP layer plays the role of blocking holes on account of its deeper HOMO. The subjacent image of Fig. 2b also shows the final structure of the prepared PHJ solar cell device by OD-VSD technology.

The OD-VSD procedure leads to multifarious films composed of different $CH_3NH_3PbI_3$ crystal sizes upon the PEDOT:PSS layer. That is, interestingly, the temperature of substrates plays an important role for the $CH_3NH_3PbI_3$ morphology. As demonstrated in the SEM images (Fig. 3a), the mean crystal size of $CH_3NH_3PbI_3$ is ~146 nm at RT (room temperature), ~173 nm at 40 °C, ~185 nm at 50 °C, ~198 nm at 60 °C, ~293 nm at 70 °C and ~ 344 nm at 80 °C, respectively. The plot of the crystal mean size as a function of substrate temperatures, depicted in Fig. 3b, suggests no linear rule. It can be recognized that much greater crystal size, rougher surface and lower coverage of the $CH_3NH_3PbI_3$ layer are determined above 60 °C. We can conclude that the variation of the $CH_3NH_3PbI_3$ crystal size is almost consistent with the temperature increase. Regardless of the temperature, the resulting $CH_3NH_3PbI_3$ (260 nm) film is approximately 2.6 times as thick as the pristine PbI_2 film (120 nm). Park *et al.* considered that the growth rate along the *c*-axis is slower than the *a*–*b* plane, and scaffolds are essential to limit the $CH_3NH_3PbI_3$ size in the conventional TiO_2 structure.[41] Nevertheless, we achieved a well controlled crystal size and morphology upon a planar PEDOT:PSS film.

In order to estimate the properties of perovskites, a group of PHJ solar cells, with the structure: ITO (100 nm)/PEDOT:PSS (30 nm)/$CH_3NH_3PbI_3$ (260 nm)/PCBM (80 nm)/BCP (10 nm)/Ag (120 nm), had been fabricated. Fig. 4a shows the average performance of the devices prepared at various substrate temperatures. The corresponding photovoltaic parameters are summarized in Table 1. In the RT case, all the values are inferior to other cases. When the temperature reached 50 to 70 °C, all the devices exhibited distinguished performances, in which the triumph PCE of 6.76% was achieved. Unfortunately, deteriorated cells at 80 °C with a PCE of 3.29% are delivered

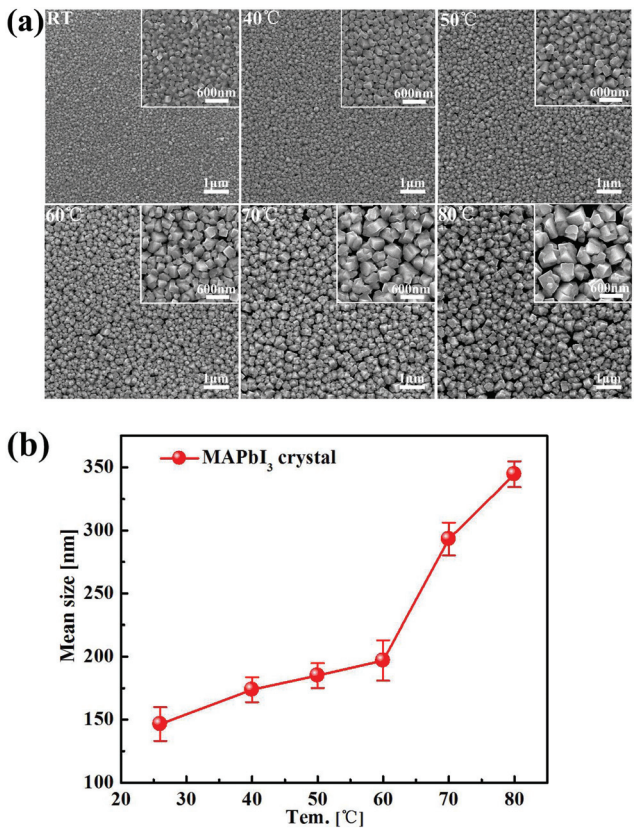

Fig. 3 (a) Top-view SEM images of the OD-VSD $CH_3NH_3PbI_3$ films upon the PEDOT:PSS layer at different substrate temperatures. (b) Plot of the mean size (nm) of $CH_3NH_3PbI_3$ crystals as a function of substrate temperatures.

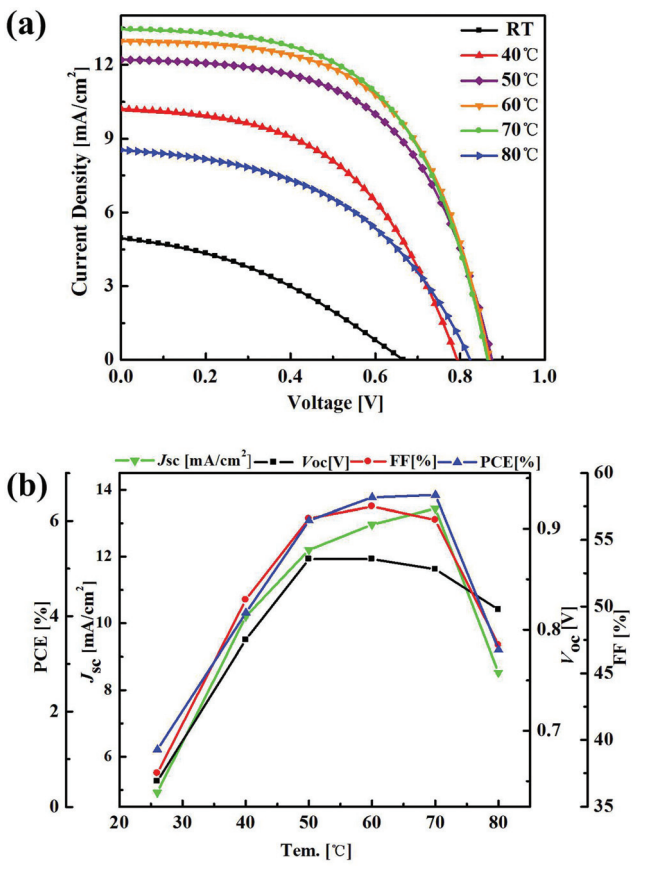

Fig. 4 (a) Current density–voltage (*J*–*V*) curves for devices fabricated at various substrate temperatures by OD-VSD technology measured under 1 sun AM 1.5G illumination. (b) The variation of J_{sc}, V_{oc}, FF and PCE as a function of the substrate temperatures.

Table 1 The average photovoltaic parameters of the ITO/PEDOT:PSS/$CH_3NH_3PbI_3$/PCBM/BCP/Ag devices by OD-VSD technology

Tem. [°C]	J_{sc} [mA cm^{-2}]	V_{oc} [V]	FF [%]	PCE [%]
RT	4.92	0.65	37.5	1.20
40	10.20	0.79	50.5	4.07
50	12.20	0.87	56.6	6.01
60	12.96	0.87	57.5	6.49
70	13.44	0.89	56.5	6.76
80	8.52	0.82	47.1	3.29

due to particularly poor coverage of perovskite films. For investigating the dependence of device performances on the temperature, the variation of each parameter as a function of substrate temperatures is plotted in Fig. 4b.

There is a positive correlation between the photovoltaic parameters and the temperature. (1) The value of FF is improved with the temperature increase, and is obviously reduced until 80 °C. This can be explained as follows: more grain boundaries at lower temperatures contribute to increasing series resistance and hence terrible FF, despite better coverage.[42] As for 80 °C, a coarse and imperfect perovskite film will lead to poor FF. (2) The variation of V_{oc} is similar to that of FF. Although the V_{oc} is determined by the difference between the LUMO of the PCBM layer and HOMO of the PEDOT:PSS layer, there still remains some factors affecting the V_{oc}. At higher temperatures, internal shunting at uncovered areas is likely caused by poorer coverage and hence results in inferior V_{oc}. At lower temperatures, what's more, the more residual PbI_2 (will be discussed later) contributes to a lower V_{oc}. (3) The improvement of J_{sc} is predominant among the overall performance enhancement along the temperature increase (except for 80 °C). The reasons for the higher temperature leading to the greater J_{sc} are confirmed for the following aspects: First and foremost, it is determined that the absorption spectra gradually enhanced at mid-long wavelengths as the substrate temperatures increase in Fig. 5a. On one hand, the utilization of visible light can be improved when the substrate temperature climbs up. Considering the similar film thickness, the increased absorption presumably results from light scattering of the larger-sized $CH_3NH_3PbI_3$ crystals of rough surface.[41,43] What's more, the increased absorption will contribute to more free carriers, which results in the corresponding J_{sc} increase.[29] On the other hand, continuous and homogenous perovskite films composed of larger-sized crystals will boost carrier transport and improve carrier-diffusion properties.[44,45]

Focused on the outstanding devices prepared at 50–70 °C, the ITO/PEDOT:PSS/$CH_3NH_3PbI_3$ films are further determined by XRD (Fig. 5b). All of the XRD patterns of 50–70 °C show a set of diffraction peaks for the tetragonal $CH_3NH_3PbI_3$ structure at 14.08°, 28.4° and 43.01°, assigned to (110), (220) and (330) planes, respectively. For 50 °C, the signal intensity at 12.6° is still evident, indicating the residual PbI_2. When the temperatures of samples are elevated to 60 °C and 70 °C, the XRD pattern of $CH_3NH_3PbI_3$ manifests that the production of

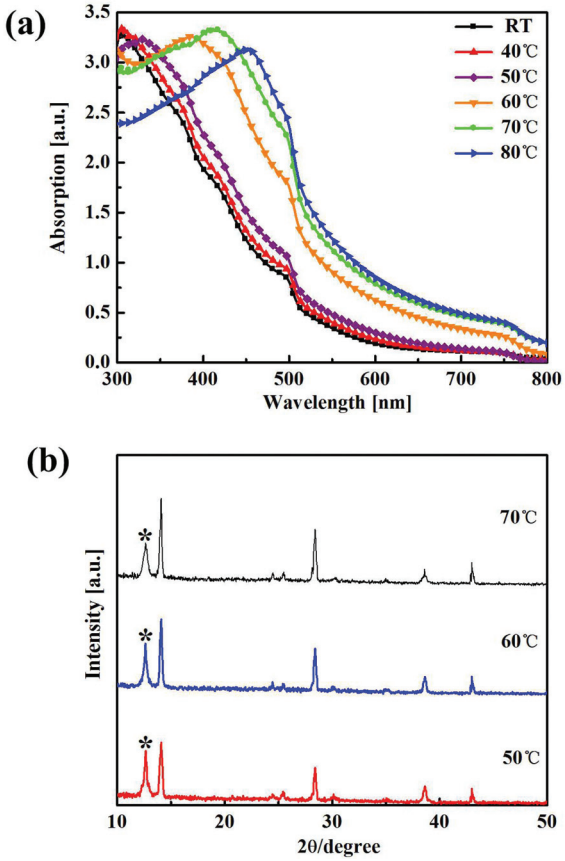

Fig. 5 (a) Absorption spectra and (b) XRD patterns (* represents the (001) plane of PbI_2) of ITO/PEDOT:PSS/$CH_3NH_3PbI_3$ films prepared by OD-VSD technology at various substrate temperatures.

perovskites is improved along with the temperature increase. In the meanwhile, pristine PbI_2 declines apparently. Hence, the crystal properties presented by XRD also account for the improvements of PCE. However, we realize that a portion of PbI_2 still remains, which is detrimental to the device performance. In order to completely transform the PbI_2 to $CH_3NH_3PbI_3$, we further attempted to develop the TD-VSD technology for improving the OD-VSD technology.

TD-VSD for perovskite solar cells

To simplify the name, OD is named for OD-VSD, while TD is named for TD-VSD. The procedure of TD is similar to that of OD. In short, after dipping into a CH_3NH_3I solution and washing, the substrates with a perovskite were heated at the same temperature for 3 min, and the procedure was conducted as the former perovskite preparation again.

For comparison, the morphology of perovskite films was first determined by SEM. Fig. 6a shows denser crystals and fewer holes of $CH_3NH_3PbI_3$ films by TD than OD at the same temperature. Actually, we can find that lots of tiny crystals fill the intervals of original larger crystals to diminish the perovskite holes in OD. The cross-sectional images (Fig. 6b) further show the prepared continuous and quasi-smooth $CH_3NH_3PbI_3$

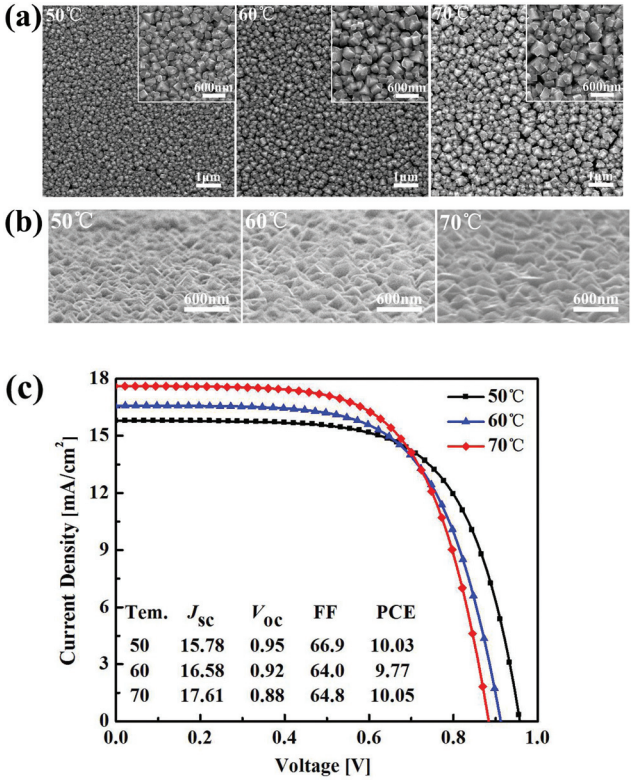

Fig. 6 (a) Top-view and (b) cross-sectional SEM images of the TD-VSD $CH_3NH_3PbI_3$ films upon the PEDOT:PSS layer at different substrate temperatures. (c) Current density–voltage (J–V) curves for devices fabricated at various substrate temperatures by TD-VSD technology measured under 1 sun AM 1.5G illumination. The inset summarizes the average parameters.

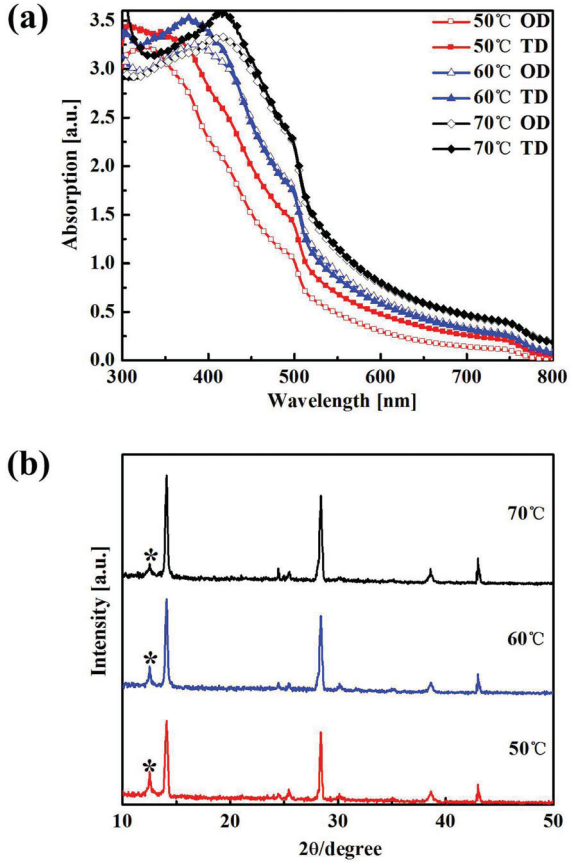

Fig. 7 (a) Absorption spectra and (b) XRD patterns (* represents the (001) plane of PbI_2) of ITO/PEDOT:PSS/$CH_3NH_3PbI_3$ films prepared by TD-VSD technology at various substrate temperatures.

films, and also the gradual enlarged crystal size as the temperature increases. Accordingly, the p-type layer (PEDOT:PSS) and the n-type layer (PCBM) will be in good contact with perovskite films, which will reduce the internal shunting as well as leakage current for the prepared device. But the film thickness still remains the same (Fig. S1†).

A group of devices of the same architecture by TD, in a similar manner to the OD procedure as described previously, were prepared to investigate the benefits of the TD procedure for the substrates at 50 °C, 60 °C and 70 °C. Fig. 6c shows the current density–voltage curves and the average photovoltaic parameters. Apparently, such solar cells exhibit amazing performances surpassing the former results by OD. At higher temperatures, a little decrease of V_{oc} would be ascribed to the tiny holes of perovskite films. Most importantly, the J_{sc} varies from 12.20 mA cm^{-2} to 15.78 mA cm^{-2} at 50 °C, from 12.96 mA cm^{-2} to 16.58 mA cm^{-2} at 60 °C, and from 13.89 mA cm^{-2} to 17.61 mA cm^{-2} at 70 °C. We then define that the ΔJ_{sc} equals to $[J_{sc}\ (TD) - J_{sc}\ (OD)]/J_{sc}$ (OD). The value of ΔJ_{sc} is 29.3% at 50 °C, 27.9% at 60 °C, and 26.8% at 70 °C, respectively, which suggests that the TD procedure could lead to a much higher short-circuit current density.

The resulting higher ΔJ_{sc} at 50 °C can also be interpreted by the absorption of perovskite films. Fig. 7a presents the absorption spectral comparison for OD and TD of the ITO/PEDOT:PSS/$CH_3NH_3PbI_3$ films. Greater enhancement of absorption covers almost all over the visible light at 50 °C. However, slighter enhancements appear only from 300 nm to 425 nm at 60 °C, and from 300 nm to 450 nm at 70 °C.

In order to further determine the benefits of TD, XRD patterns of ITO/PEDOT:PSS/$CH_3NH_3PbI_3$ films fabricated by TD are shown in Fig. 7b. Compared with the XRD patterns of OD, enhancement of the intensity of $CH_3NH_3PbI_3$ is much strong, which indicates almost adequate conversion of PbI_2. The improvement of J_{sc} is also observed, and the favorable crystals of perovskites prepared at higher temperatures are also consistent with the SEM images.

Mechanism

To further demonstrate the nature of perovskite formation, another group of perovskites by dipping the substrates covered with PbI_2 at 50 °C, 60 °C, 70 °C, and even 80 °C three times was prepared. The third dipping is denoted as T'D.

Distinct variation of absorption spectra can be found between OD and T'D in Fig. 7a. But almost no obvious

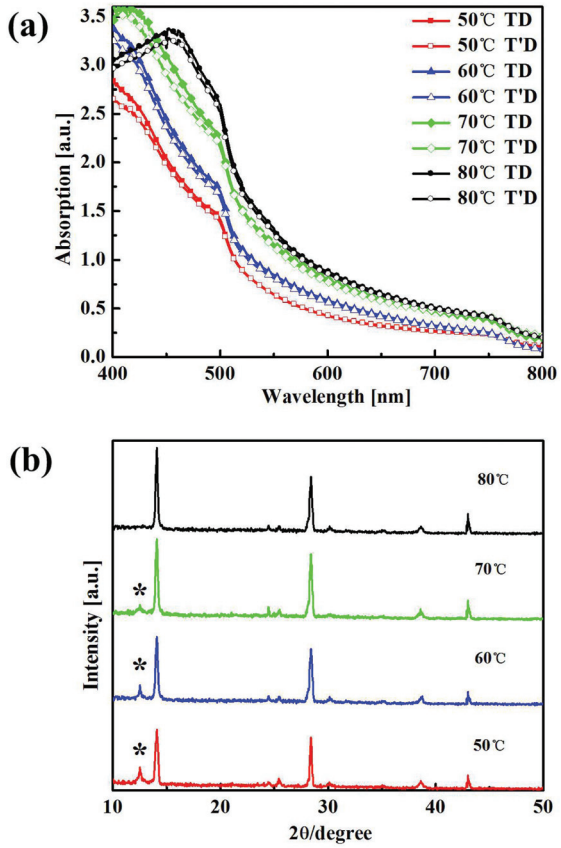

Fig. 8 (a) Absorption spectra and (b) XRD patterns (* represents the (001) plane of PbI_2) of ITO/PEDOT:PSS/$CH_3NH_3PbI_3$ films prepared by the T'D procedure at various substrate temperatures.

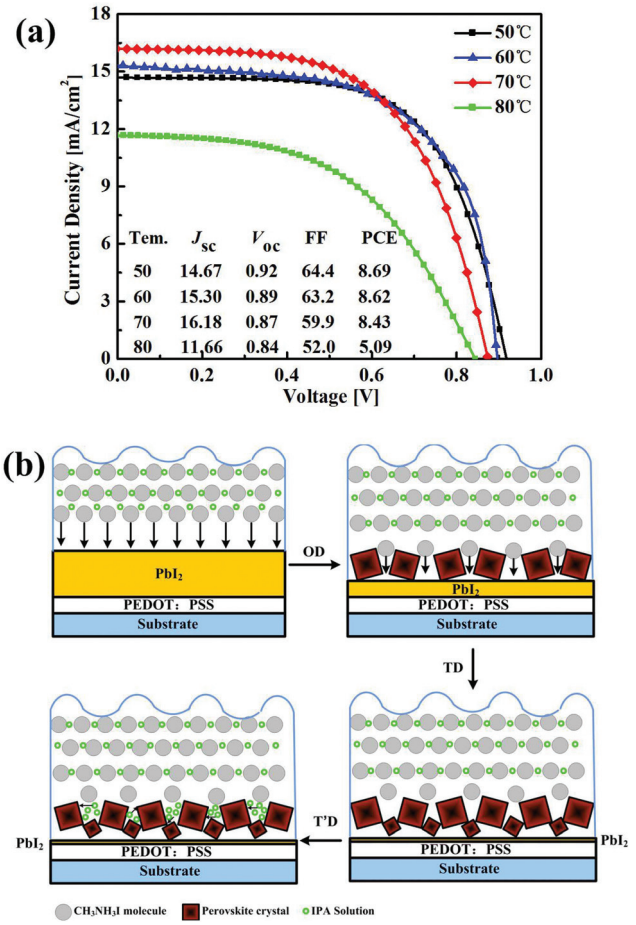

Fig. 9 (a) Current density–voltage (J–V) curves for devices fabricated at various substrate temperatures by the T'D procedure measured under 1 sun AM 1.5G illumination. The inset summarizes the average parameters. (b) Illustration of the mechanism stages for perovskite formation.

variation appears between TD and T'D in Fig. 8a. This odd result reminds us that the perovskite formation may be limited by some factors.

Fig. 8b shows XRD patterns of T'D at various substrate temperatures. The corresponding intensities of diffraction peaks can be found in Table S1.† From OD to TD, all the intensities of 12.6° decline apparently, meanwhile the intensities of 14.08° increase strongly. This indicates that the residual PbI_2 was diminished to some extent. From TD to T'D, the intensities at 12.6° nearly remain but the diffraction peaks of perovskites all decrease slightly. Speculated from the XRD patterns, the conversion degree into perovskites has been aggravated by TD, but ceased even reduced by T'D. And the PbI_2 will be completely transformed into perovskites at 80 °C. Similarly, coverage rates are improved from OD to TD, but almost remain from TD to T'D from the top-view SEM images (Fig. S2†).

The devices with the same layout were prepared to determine the effect of T'D. Fig. 9a presents the current density–voltage curves and the average photovoltaic parameters. However, frustrating performances were obtained in comparison with TD. This unfavorable result indicates that the perovskite film made by T'D is really deteriorated, which is in accordance with film characterization. Though 80 °C will lead to complete conversion, the terrible film surface destroys the device. We can infer that a better interface is more beneficial for device performance than little PbI_2.

From all the former results, the perovskite mechanism can be speculated in following aspects:

(1) For the OD procedure, when the substrates at different temperatures were immersed into a CH_3NH_3I solution, the CH_3NH_3I molecules immediately react with the PbI_2 film. Due to the more condensed nature of the vapor PbI_2 film, the reaction degree and rate will be limited but improved by the use of a suitable temperature. However all the PbI_2 still cannot be completely transformed into perovskite.

(2) For the TD procedure, the upper layers of the substrate are composed of perovskite–PbI_2 films. There are lots of major holes as well as intervals existing between the large-sized crystals of perovskite. The CH_3NH_3I molecules will filter into these defects and continue to react with the residual PbI_2 films. Consequently, lots of tiny crystals appear between the bigger crystals regardless of little corrosion by IPA.

(3) For the T'D procedure, the perovskite crystals are denser and show almost no defects. The CH_3NH_3I molecules hardly meet with the little residual PbI_2 (except at 80 °C). What's more, an excess IPA solution may partially corrode the perovskite by TD due to the substrate's third immersion. The eventual results also support the possible reason.

Regardless of the complicated factors by now, this primary mechanism is established. As an example, Fig. 9b shows the illustration of the mechanism stages for PbI_2 conversion into perovskites.

Device optimization

Finally, we maintained the architecture to optimize the solar cells by adjusting the PbI_2 thickness (120 nm) with the TD procedure. The average device performances are shown in Table 2. All the devices prepared with 150 nm PbI_2 exhibit better performances, especially higher J_{sc}. The maximum J_{sc} of 18.58 mA cm^{-2} has almost been comparable to the J_{sc} of the excellent p-i-n PHJ devices reported (from 16.12 to 19.2 mA cm^{-2}).[24,29,30] What's more, the devices fabricated with 150 nm PbI_2 by TD manifested good FF (above 60%) as well as high V_{oc} (about 1.0 V), which can be attributed to the robust interfaces between the perovskite films and the PCBM layers.

Fig. 10a demonstrates the current density–voltage curves of the champion solar cells, achieving at 50 °C, measured under 1 sun AM 1.5G illumination and in the dark. The optimizing highest PCE of 11.77% was realized, yielding a J_{sc} of 17.28 mA cm^{-2}, a V_{oc} of 1.05 V and a FF of 64.8%, respectively. Histograms of the cell performance characteristics are shown Fig. S3.† It is noted that the relative standard deviation of the PCE was only 0.27, which indicates excellent reproducibility of the devices by TD-VSD technology. The high open-circuit potential also implies negligible surface defects and sub-bandgap states in the perovskite film.[30] Meanwhile, the hysteresis of the scan process, existing in our devices (Fig. S4†), shows 11% deviation of PCE from reverse to forward. The incident photon-to-current conversion efficiency (IPCE) spectrum (Fig. 10b) exhibits generation of the photocurrent starting at 800 nm, in agreement with the bandgap of the $CH_3NH_3PbI_3$, and reaches peak values in the short-wavelength region of the visible spectrum. The integrated current density derived from the EQE spectra in Fig. 10b is close to the J_{sc} measured under simulated sunlight.

Table 2 The average photovoltaic parameters of the ITO/PEDOT:PSS/$CH_3NH_3PbI_3$/PCBM/BCP/Ag devices by OD-VSD technology

Tem. [°C]	PbI_2 thickness [nm]	J_{sc} [mA cm^{-2}]	V_{oc} [V]	FF [%]	PCE [%]
50	90	15.14	0.91	63.8	8.79
	150	16.66	1.03	65.1	11.17
60	90	15.83	0.88	61.7	8.59
	150	17.12	1.00	62.1	10.63
70	90	16.95	0.84	59.6	8.48
	150	18.58	0.98	60.3	10.97

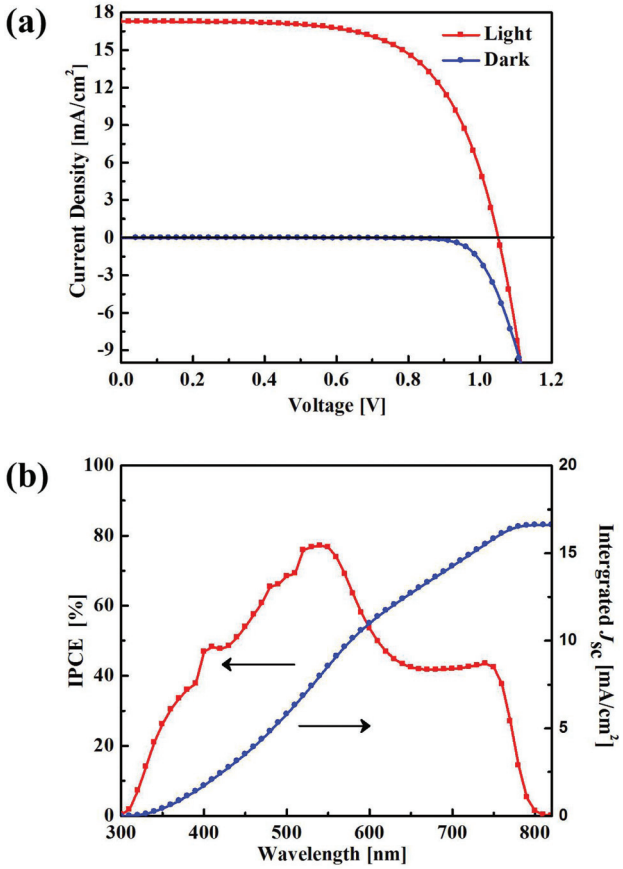

Fig. 10 (a) Current density–voltage (J–V) curves and (b) IPCE spectrum for champion solar cells fabricated at 50 °C by TD-VSD technology measured under 1 sun AM 1.5G illumination and in the dark.

Conclusion

Highly efficient inverted PHJ perovskite solar cells were achieved and optimized using a novel TD-VSD technology. We emphasized the effect of substrate (covered with PbI_2) temperatures on the resulting $CH_3NH_3PbI_3$ crystal sizes and uniformity, and found that large-sized crystals will result in stronger absorption at mid-long wavelengths. Furthermore, the primary mechanism of perovskite formation is established by employing dipping substrates for different times. It is notable that the optimized procedure revealed more sufficient conversion of VD PbI_2 films. When an appropriate temperature is established, the favorable $CH_3NH_3PbI_3$ films with fewer defects would support better interfaces and improve carrier transport. For this controlled thickness and morphology of $CH_3NH_3PbI_3$ films, a champion solar cell prepared in this way showed the highest PCE of 11.77%.

Experimental

Preparation of materials

Methylammonium iodide (MAI) was synthesized according to a previous study.[8] In brief, 24 mL methylamine solution

(33 wt% in ethanol, Sigma Aldrich) and 10 mL hydriodic acid (57 wt% in water, Sigma Aldrich) were diluted with 100 mL ethanol in a 250 mL round bottom flask by constant stirring at 0 °C for 2 hours. The precipitate of CH_3NH_3I was obtained by rotary evaporation at 40 °C and washed with dry diethyl ether until the solid became white. The final product was dried at 60 °C in a vacuum oven for 24 h. PbI_2 (99.999 wt%) was purchased from Alfa. PEDOT:PSS (CLEVIOS PH 1000) solution and PCBM were acquired from Haraeus and Solenne, respectively.

Fabrication of solar cells

(1) Pretreatment: ITO glass substrates were cleaned sequentially with a detergent, pure water, and acetone for 20 min. The dried substrates were treated with ultraviolet ozone plasma for 5 min for further cleaning. PEDOT:PSS solutions (dissolved with deionized water in a mixture ratio of 1 : 3) were spun at 1000 rpm for 30 s and annealed at 120 °C for 20 min.

(2) Perovskite fabrication: for OD-VSD, we transferred the substrates coated with PEDOT:PSS to a vacuum chamber. The PbI_2 films of 90 nm, 120 nm or 150 nm were sublimated under a pressure of 10^{-5} mbar at a rate of 1.0 Å s^{-1} and the resulting substrates were placed into a N_2-filled glovebox, maintained at room temperature, or heated for 2 min at 40, 50, 60, 70 and 80 °C, respectively; the ITO/PEDOT:PSS/PbI_2 substrates were immersed into a CH_3NH_3I solution (10 mg mL^{-1} in 2-propanol) for 1 min, followed by washing with 2-propanol and dichloromethane. For TD-VSD, this group was implemented by the same process as OD-VSD. Moreover, the prepared perovskite films were again heated, dipped and washed. For T'D-VSD, the same process was repeated for the third time.

(3) Device achievements: almost 80 nm p-type films were deposited by spin-coating a PCBM solution (30 mg ml^{-1} in chlorobenzene) at 2000 rpm for 30 s. Eventually, the devices were completed by consecutively vacuum depositing BCP (10 nm) and Ag cathode (120 nm) under 10^{-5} mbar.

Characterization

Perovskite films for absorption measurements, SEM, AFM and XRD were prepared under the same fabrication conditions for the layer structures configured as: glass substrate/ITO/PEDOT:PSS/$CH_3NH_3PbI_3$. The absorption spectra were acquired on a UV-vis spectrophotometer (Fluoromax 4, HORIBA Jobin Yvon, USA). The morphology was investigated by scanning electron microscopy (SEM) (Quanta 250, FEI). The crystalline structures were analysed by X-ray diffraction (XRD) (D/MAX-2400, Rigaku, Japan) with Cu Kα radiation.

Device characteristics were evaluated in ambient air under an AAA solar simulator (XES-301S, SAN-EI Electric. Co. Ltd), AM 1.5G illumination with an intensity of 100 mW cm^{-2} (1 sun, calibrated with a NREL-traceable KG5 filtered silicon reference cell). Meanwhile, the current density–voltage (J–V) curves were measured using a Keithley digital source meter (Model 2602). The scan rates of the planar heterojunction perovskite solar cell current–voltage curves was 0.5 V s^{-1} starting from −0.1 V to 1.2 V. The incident photon-to-current conversion efficiency (IPCE) spectra were obtained using a solar cell quantum efficiency measurement system (SolarCellScan 100, Zolix instruments. Co. Ltd). The area of each device, calibrated with a shadow mask, was 9.00 mm^2.

Acknowledgements

This work was financially supported by the Basic Research Program of China (2013CB328705), the National Natural Science Foundation of China (Grant No. 61275034), and the PhD Programs Foundation of Ministry of Education of China (Grant No. 20130201110065). The SEM work was done at International Center for Dielectric Research (ICDR), Xi'an Jiaotong University, Xi'an, China; the authors also thank Ms Dai for her help in using SEM.

Notes and references

1 A. Kojima, K. Teshima, Y. Shirai and T. Miyasaka, *J. Am. Chem. Soc.*, 2009, **131**, 6050–6051.
2 S. D. Stranks, G. E. Eperon, G. Grancini, C. Menelaou, M. J. P. Alcocer, T. Leijtens, L. M. Herz, A. Petrozza and H. J. Snaith, *Science*, 2013, **342**, 341–344.
3 G. Xing, N. Mathews, S. Sun, S. S. Lim, Y. M. Lam, M. Gräztel, S. Mhaisalkar and T. C. Sum, *Science*, 2013, **342**, 344–347.
4 T. Leijtens, J. Lim, J. Teuscher, T. Park and H. J. Snaith, *Adv. Mater.*, 2013, **25**, 3227–3233.
5 C. Wehrenfennig, G. E. Eperson, M. B. Johnston, H. J. Snaith and L. M. Herz, *Adv. Mater.*, 2014, **26**, 1584–1589.
6 H. Zhou, Q. Chen, G. Li, S. Luo, T.-B. Song, H.-S. Duan, Z. Hong, J. You, Y. Liu and Y. Yang, *Science*, 2014, **345**, 542–546.
7 H. S. Kim, C. R. Lee, J. H. Im, K. B. Lee, T. Moehl, A. Marchioro, S. J. Moon, R. Humphry-Baker, J. H. Yum, J. E. Moser, M. Gräztel and N. G. Park, *Sci. Rep.*, 2012, **2**, 591.
8 M. M. Lee, J. Teuscher, T. Miyasaka, T. N. Murakami and H. J. Snaith, *Science*, 2012, **338**, 643–647.
9 J. T.-W. Wang, J. M. Ball, E. M. Barea, A. Abate, J. A. Webber, J. Huang, M. Saliba, I. Mora-Sero, J. Bisquert, H. J. Snaith and R. J. Nicholas, *Nano Lett.*, 2014, **14**, 724–730.
10 G. E. Eperon, V. M. Burlakov, P. Docampo, A. Goriely and H. J. Snaith, *Adv. Funct. Mater.*, 2014, **24**, 151–157.
11 A. Dualeh, N. Tetreault, T. Moehl, P. Gao, M. K. Nazeeruddin and M. Gräztel, *Adv. Funct. Mater.*, 2014, **24**, 3250–3258.
12 J. M. Ball, M. M. Lee, A. Hey and H. J. Snaith, *Energy Environ. Sci.*, 2013, **6**, 1739.
13 N.-G. Park, *J. Phys. Chem. Lett.*, 2013, **4**, 2423–2329.
14 J.-Y. Jeng, Y.-F. Chiang, M.-H. Lee, S.-R. Peng, T.-F. Guo, P. Chen and T.-C. Wen, *Adv. Mater.*, 2013, **25**, 3727–3732.
15 J. You, Z. Hong, Y. Yang, Q. Chen, M. Cai, T.-B. Song, C.-C. Chen, S. Lu, Y. Liu, H. Zhou and Y. Yang, *ACS Nano*, 2014, **8**, 1674–1680.

16 C. Roldan-Carmona, O. Malinkiewicz, A. Soriano, G. M. Espellargas, A. Garcia, P. Reinecke, T. Kroyer, M. L. Dar, M. K. Nazeeruddin and H. J. Bolink, *Energy Environ. Sci.*, 2014, **7**, 994–997.
17 Y.-F. Chiang, J.-Y. Jeng, M.-H. Lee, S.-R. Peng, P. Chen, T.-F. Guo, T.-C. Wen, Y.-J. Hsu and C.-M. Hsu, *Phys. Chem. Chem. Phys.*, 2014, **16**, 6033–6040.
18 J.-Y. Jeng, K.-C. Chen, T.-Y. Chiang, P.-Y. Lin, T.-D. Tsai, Y.-C. Chang, T.-F. Guo, P. Chen, T.-C. Wen and Y.-J. Hsu, *Adv. Mater.*, 2014, **26**, 4107–4133.
19 K.-C. Wang, P.-S. Shen, M.-H. Li, S. Chen, M.-W. Lin, P. Chen and T.-F. Guo, *ACS Appl. Mater. Interfaces*, 2014, **6**, 11851–11858.
20 A. S. Subbiah, A. Halder, S. Ghosh, N. Mahuli, G. Hodes and S. K. Sarkar, *J. Phys. Chem. Lett.*, 2014, **5**, 1748–1753.
21 Z. Wu, S. Bai, J. Xiang, Z. Yuan, Y. Yang, W. Cui, X. Gao, Z. Liu, Y. Jin and B. Sun, *Nanoscale*, 2014, **6**, 10505–10510.
22 L. Hu, J. Peng, W. Wang, Z. Xia, J. Yuan, J. Lu, X. Huang, W. Ma, H. Song, W. Chen, Y.-B. Cheng and J. Tang, *ACS Photonics*, 2014, **1**, 547–553.
23 Z. Zhu, Y. Bai, T. Zhang, Z. Liu, X. Long, Z. Wei, Z. Wang, L. Zhang, J. Wang, F. Yan and S. Yang, *Angew. Chem., Int. Ed.*, 2014, **53**, 12571–12575.
24 J. Seo, S. Park, Y. C. Kim, N. J. Jeon, J. H. Noh, S. C. Yoon and S. I. Seok, *Energy Environ. Sci.*, 2014, **7**, 2642–2646.
25 Q. Wang, Y. Shao, Q. Dong, Z. Xiao, Y. Yuan and J. Huang, *Energy Environ. Sci.*, 2014, **7**, 2359–2365.
26 H.-B. Kim, H. Choi, J. Jeong, S. Kim, B. Walker, S. Song and J. Y. Kim, *Nanoscale*, 2014, **6**, 6670–6683.
27 C. Zuo and L. Ding, *Nanoscale*, 2014, **6**, 9935–9938.
28 C.-W. Chen, H.-W. Kang, S.-Y. Hsiao, P.-F. Yang, K.-M. Chiang and H.-W. Lin, *Adv. Mater.*, 2014, **26**, 6647–6652.
29 O. Malinkiewicz, C. Roldan-Carmona, A. Soriano, E. Bandiello, L. Camacho, M. K. Nazeeruddin and H. J. Bolink, *Adv. Energy Mater.*, 2014, **4**, 1400345.
30 O. Malinkiewicz, A. Yella, Y. H. Lee, G. M. Espallargas, M. Gräztel, M. K. Nazeeruddin and H. J. Bolink, *Nat. Photonics*, 2014, **8**, 128–132.
31 Q. Lin, A. Armin, R. C. R. Nagiri, P. L. Burn and P. Meredith, *Nat. Photonics*, 2015, **9**, 106–112.
32 J. Burschka, N. Pellet, S.-J. Moon, R. Humphry-Baker, P. Gao, M. K. Nazeeruddin and M. Gräztel, *Nature*, 2013, **499**, 316–319.
33 M. Liu, M. B. Johnston and H. J. Snaith, *Nature*, 2013, **501**, 395–398.
34 P.-W. Liang, C.-Y. Liao, C.-C. Chueh, F. Zuo, S. T. Williams, X.-K. Xin, J. Lin and A. K.-Y. Jen, *Adv. Mater.*, 2014, **26**, 3748–3754.
35 B. Conings, L. Baeten, D. D. Dobbelaere, J. D'Haen, J. Manca and H.-G. Boyen, *Adv. Mater.*, 2014, **26**, 2041–2046.
36 Y. Wu, A. Aslam, X. Yang, C. Qin, J. Liu, K. Zhang, W. Peng and L. Han, *Energy Environ. Sci.*, 2014, **7**, 2934–2938.
37 L. Dou, J. You, Z. Hong, Z. Xu, G. Li, R. A. Street and Y. Yang, *Adv. Mater.*, 2013, **25**, 6642–6671.
38 N. R. Armstrong, W. Wang, D. M. Alloway, D. Placencia, E. Ratcliff and M. Brumbach, *Macromol. Rapid Commun.*, 2009, **30**, 717–731.
39 A. L. Ayzner, C. J. Tassone, S. H. Tolbert and B. J. Schwartz, *J. Phys. Chem. C*, 2009, **113**, 20050–20060.
40 D. Bi, A. M. El-Zohry, A. Hagfeldt and G. Boschloo, *ACS Appl. Mater. Interfaces*, 2014, **6**, 18751–18757.
41 J.-H. Im, I.-H. Jang, N. Pellet, M. Gräztel and N. G. Park, *Nat. Nanotechnol.*, 2014, **9**, 927–932.
42 L. M. Frass, *J. Appl. Phys.*, 1978, **49**, 871–875.
43 D. Liu and T. L. Kelly, *Nat. Photonics*, 2014, **8**, 133–138.
44 L. Zheng, Y. Ma, S. Chu, S. Wang, B. Qu, L. Xiao, Z. Chen, Q. Gong, Z. Wu and X. Hou, *Nanoscale*, 2014, **6**, 8171–8176.
45 T. Baikie, Y. Fang, J. M. Kadro, M. Schreyer, F. Wei, S. G. Mhaisalkar, M. Graetzel and T. J. White, *J. Mater. Chem. A*, 2013, **1**, 5628–5641.